



Power Electronic Systems
Laboratory

© 2021 IEEE

Proceedings of the 24th International Conference on Electrical Machines and Systems (ICEMS 2021),
Gyeongju, Korea, October 31-November 3, 2021

“Pushing Power Through Walls” – Wireless Power Transfer Through Stainless Steel

S. Miric,
M. Tatic,
J. Huber,
D. Bortis,
J. W. Kolar

Personal use of this material is permitted. Permission from IEEE must be obtained for all other uses, in any current or future media, including reprinting/republishing this material for advertising or promotional purposes, creating new collective works, for resale or redistribution to servers or lists, or reuse of any copyrighted component of this work in other works.



Eidgenössische Technische Hochschule Zürich
Swiss Federal Institute of Technology Zurich

“Pushing Power Through Walls” – Wireless Power Transfer Through Stainless Steel

Spasoje Mirić, Mina Tatić, Jonas Huber, Dominik Bortis and Johann W. Kolar
 ETH Zurich, Power Electronic Systems Laboratory
 Zurich, Switzerland
 miric@lem.ee.ethz.ch

Abstract—This paper focuses on wireless power transfer (WPT) through an electrically conductive stainless steel (SS) enclosure necessary for high-purity environments such as required for chemical or pharmaceutical industry. The alternating electromagnetic field penetrates the SS and induces eddy currents that are opposing the field of the primary coil and reduce the coupling and efficiency of the WPT system. Considering a WPT system with E-core geometry, we show how to simplify its modeling with an equivalent circuit approach, while including SS enclosure effects. We show that with such WPT system, special care must be taken when designing resonant compensation, because compensating self-inductances, as typically done for WPT systems, results in larger SS losses than if stray inductances are compensated. Additionally, we show that there is an optimal number of turns, for the primary and secondary windings, which depends on the nominal output power and voltage. Finally, the proposed model is verified with measurements on a hardware demonstrator built with two 0.5 mm thick SS walls that emulate the enclosure. The demonstrator is designed for 50 V output voltage, equal numbers of primary and secondary side turns and is operated at 2250 Hz up to 70 W output power.

Index Terms—Wireless Power Transfer, WPT, Inductive Power Transfer, IPT, Metal Enclosure, Low Frequency WPT, Resonant Compensation, Power Control.

I. INTRODUCTION

Wireless power transfer (WPT) is extensively analyzed in literature [1] and it is successfully implemented in many practical applications, ranging from kilowatt systems for electrical vehicle charging [2] down to supplying implanted medical devices [3], [4] with several watts or milliwatts. In conventional WPT systems the primary-side and secondary-side coils are realized as air coils with litz wire, and ferrite cores may be used to provide some flux guidance, better coupling and shielding. There, typically frequency-dependent parasitic skin and proximity effects are not predominate and high frequencies of the alternating field (tens of kHz, typically 85 kHz) can be used and despite high frequencies high transmission efficiencies of $> 90\%$ can be achieved.

In the chemical or pharmaceutical industries, supplied equipment often needs protection and encapsulation due to ultra-high purity demands or exposure to aggressive environments. For example, in the pharmaceutical industry, machines are preferably fully enclosed in stainless-steel (SS) to prevent contamination of chemical processes, e.g. by particles resulting from abrasion, and to facilitate cleaning/disinfection with aggressive detergents. Various machines and actuators in high purity industrial environments are usually supplied via cable or cable carriers, which are difficult to fully seal, protect from the environment, and keep thoroughly clean. Furthermore, in case there is continuous motion, the lifetime of the cables and cable carriers is limited. Thus, a WPT system with its primary-side

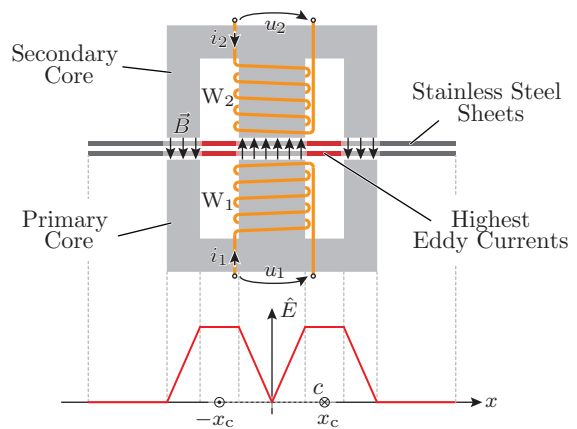


Fig. 1: Analyzed WPT system with E-cores on the primary and secondary side with two SS sheets (emulating the primary-side and secondary-side enclosures) between them. Due to the AC flux density, the induced voltage’s amplitude \hat{E} has the indicated profile, i.e., it is proportional to the operating frequency and the integral of the flux density \vec{B} over the area defined by a closed contour c around the E-core symmetry axis in the SS planes.

TABLE I: SS WPT system nominal data.

Input Voltage	Output Voltage	Output Power
$\hat{U}_1 = 50 \text{ V}$	$\hat{U}_2 = 50 \text{ V}$	$P_2 = 50 \text{ W}$

and secondary-side coils and power electronics fully enclosed in SS would provide a viable solution.

Therefore, we consider an arrangement for WPT through SS as shown in **Fig. 1**, where two SS sheets between the primary-side and the secondary-side emulate full SS enclosures. Due to the electric conductivity of SS (measured at room temperature to be $\approx 1.3 \text{ MS/m}$), eddy currents are induced, causing issues such as severe impact on transmission efficiency [5]–[8] and limitation of the feasible operating frequency range [9]. Similar detrimental effects of conductive enclosures on performance can be seen in eddy current sensors embedded in metal cases [10]. To address these issues, in this paper we analyze in detail modeling, operation, resonant compensation, and power flow control of the SS WPT system shown in **Fig. 1**. First, we derive a simple and effective electrical circuit model which considers the impact of the eddy currents induced in the SS enclosures, and we determine its parameters from 3D FEM simulations, as described in **Sec. II**. In **Sec. III** we show that resonant compensation should not consider self-inductances and that the stray inductances should be compensated instead. **Sec. IV** shows that depending on the design output power and voltage, there is an optimum number of turns for the primary

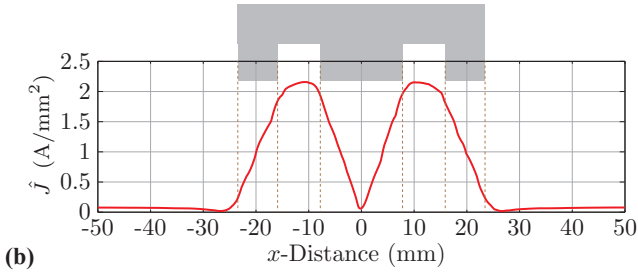
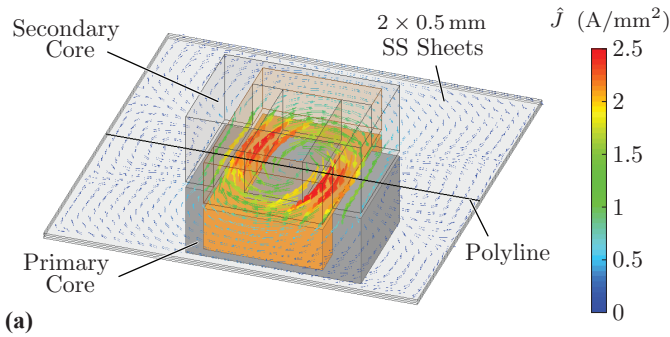


Fig. 2: (a) 3D FEM simulation of the eddy current distribution in the SS for a current excitation of the primary (100 Aturns) and the secondary (0 Aturns) winding, at 1kHz excitation frequency. (b) Current density amplitude along the polyline through the middle of the lower SS sheet (closer to the primary winding). For the geometry parameters see **Fig. 3**.

and secondary winding that maximizes the WPT efficiency. Based on this, a hardware prototype is built and presented in **Sec. V**. With small signal impedance measurements on the prototype, we verify the proposed circuit model and 3D-FEM-simulation-based parametrization. In addition, we characterize high-frequency effects in the windings and include them in the circuit model. We determine an optimum excitation frequency range and conduct power measurements which verify the validity of the proposed circuit model. Furthermore, we discuss two output power control methods: (1) change of the input voltage and (2) change of the equivalent load resistance. Finally, **Sec. VI** concludes the paper and gives an outlook of further research.

II. MODELING OF THE SS WPT SYSTEM

Due to the alternating flux density \vec{B} in the air gap of the SS WPT system depicted in **Fig. 1**, eddy currents are induced in the SS. Those eddy currents form loops around the E-cory symmetry axis similar to the loop c indicated in **Fig. 1**, which can be seen better in **Fig. 2(a)**, where 3D FEM simulation (ANSYS) results are given. The eddy current density amplitude \hat{J} is proportional to the induced voltage \hat{E} along a certain contour and inversely proportional to the contour's ohmic resistance, which results in the eddy current density amplitude \hat{J} shown in **Fig. 2(b)** for an exemplary cross section. The detailed geometry and geometrical parameters of the analyzed SS WPT system are given in **Fig. 3**.

The current density amplitude distribution \hat{J} , given in **Fig. 2(b)**, reaches its maximum value between the limbs of the core, due to the highest induced voltages along the corresponding contours (see \hat{E} in **Fig. 1**). Having in mind such current distribution, its impact onto the SS WPT system can be modeled with an equivalent WPT system shown in

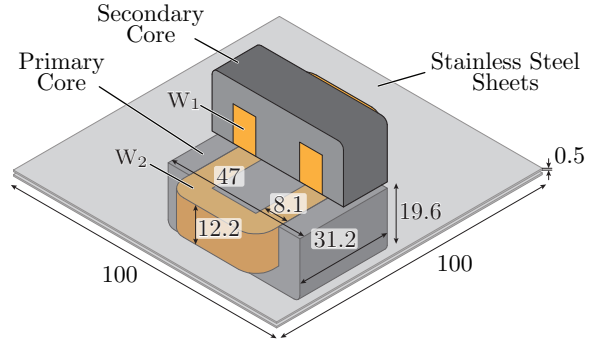


Fig. 3: Dimensions (in millimeters) of the analyzed WPT system. The primary and secondary cores are realized by stacking two E 47/20/16 N87 ferrite cores, cf. [11]. The mechanical air gap between the SS sheets (0.5 mm thickness) is 0.5 mm and the distance of the cores from the SS is also 0.5 mm. Therefore, the total magnetic air gap is 2.5 mm. The relative permeability of the SS is $\mu_{r,SS} = 1$, the assumed conductivity of copper is 58.7 MS/m, and the winding fill factor is 0.4 which takes influence on the winding resistance calculation.

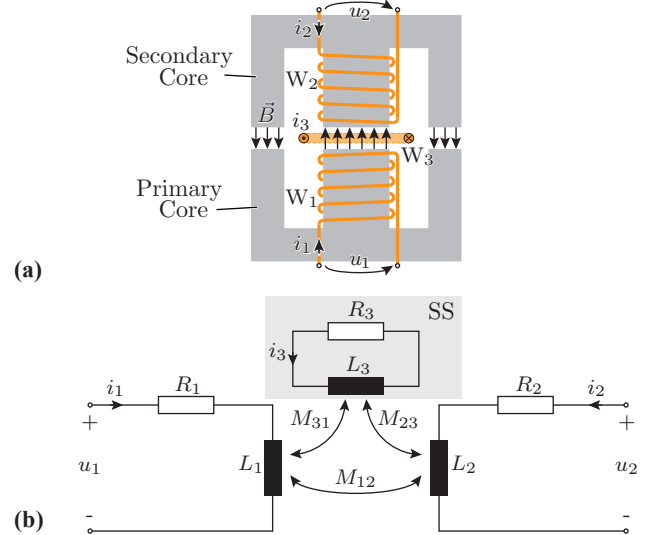


Fig. 4: (a) Analyzed WPT system from **Fig. 1** where the SS sheets are replaced by a single turn winding W_3 . (b) Three-winding transformer equivalent circuit used to model the WPT system from (a), which includes the third short-circuited winding with the equivalent SS resistance R_3 .

Fig. 4(a). More specifically, the SS plates are completely removed and replaced with a single turn winding W_3 in the SS plane which allows to represent the system with a three-winding transformer circuit, cf. **Fig. 4(b)**. Note that a similar circuit has been used to model the shielding effect of metal plates for a WPT system in [12]. The two main windings, i.e., primary winding W_1 and secondary winding W_2 , are coupled with mutual inductance M_{12} , but they are also coupled with the third winding W_3 (modeling the SS), with mutual inductances M_{31} and M_{23} , respectively. Due to these couplings, a voltage across R_3 , which emulates the residual SS resistance seen by the eddy currents, is induced and a certain power is dissipated instead of being transferred to the output. Note that this power is equal to the losses in the SS. To simplify the analysis of the system, an equivalent circuit with leakage and mutual inductances is derived, cf. [13]. For

its derivation, the following set of voltage balance equations is used

$$\begin{aligned} u_1 &= R_1 i_1 + L_1 \frac{di_1}{dt} + M_{12} \frac{di_2}{dt} + M_{31} \frac{di_3}{dt}, \\ u_2 &= R_2 i_2 + L_2 \frac{di_2}{dt} + M_{12} \frac{di_1}{dt} + M_{23} \frac{di_3}{dt}, \\ 0 &= R_3 i_3 + L_3 \frac{di_3}{dt} + M_{23} \frac{di_2}{dt} + M_{31} \frac{di_1}{dt}, \end{aligned} \quad (1)$$

where the voltage drops due to winding resistances $R_{\{1,2,3\}}$, and the voltage components due to self-inductances $L_{\{1,2,3\}}$ and mutual inductances $M_{\{12,23,31\}}$ are considered. The mutual inductances $M_{\{12,23,31\}}$ are related to each other through the number of turns of the primary N_1 , the secondary N_2 , and the third winding N_3 (note that for the analysis of the SS WPT system $N_3 = 1$) as

$$M_{12} = N_1 N_2 \cdot M_0 \quad M_{23} = N_2 N_3 \cdot M_0 \quad M_{31} = N_3 N_1 \cdot M_0 \quad (2)$$

M_0 denotes the mutual inductance per turn, i.e., for the case $N_1 = N_2 = N_3 = 1$. Therefore, in (2) equal mutual inductances (for equal number of turns of all three windings) between the primary winding and the secondary winding, the secondary winding and the SS winding, and the SS winding and the primary winding, are assumed. This assumption is justified in **Fig. 5**, where it is shown that due to symmetry reasons it cannot happen that the coupling between W_2 and W_3 is different from the coupling between W_2 and W_1 , since flux lines like Φ_{23} (denoted in red, cf. **Fig. 5**) cannot exist as this would violate the magnetic symmetry. Note that the stray field lines (that are linked to only one winding) are not considered in this analysis. If turns ratios are defined as $n = N_1/N_2$ and $m = N_1/N_3$, (1) can be written as

$$\begin{aligned} u_1 &= R_1 i_1 + L_1 \frac{di_1}{dt} + \underbrace{nM_{12}}_{=M} \frac{d \frac{i_2}{n}}{dt} + \underbrace{mM_{31}}_{=M} \frac{d \frac{i_3}{m}}{dt}, \\ nu_2 &= n^2 R_2 \frac{i_2}{n} + n^2 L_2 \frac{d \frac{i_2}{n}}{dt} + \underbrace{nM_{12}}_{=M} \frac{di_1}{dt} + \underbrace{nmM_{23}}_{=M} \frac{d \frac{i_3}{m}}{dt}, \\ 0 &= m^2 R_3 \frac{i_3}{m} + m^2 L_3 \frac{d \frac{i_3}{m}}{dt} + \underbrace{nmM_{23}}_{=M} \frac{d \frac{i_2}{n}}{dt} + \underbrace{mM_{31}}_{=M} \frac{di_1}{dt}, \end{aligned} \quad (3)$$

where, using (2) and the turns ratios n and m , it is trivial to show that

$$n M_{12} = m M_{31} = nm M_{23} = N_1^2 M_0 = M. \quad (4)$$

Equation set (3) now can be rewritten as:

$$\begin{aligned} u_1 &= R_1 i_1 + (L_1 - M) \frac{di_1}{dt} + M \frac{d}{dt} \left(i_1 + \frac{i_2}{n} + \frac{i_3}{m} \right), \\ nu_2 &= n^2 R_2 \frac{i_2}{n} + (n^2 L_2 - M) \frac{d \frac{i_2}{n}}{dt} + M \frac{d}{dt} \left(i_1 + \frac{i_2}{n} + \frac{i_3}{m} \right), \\ 0 &= m^2 R_3 \frac{i_3}{m} + (m^2 L_3 - M) \frac{d \frac{i_3}{m}}{dt} + M \frac{d}{dt} \left(i_1 + \frac{i_2}{n} + \frac{i_3}{m} \right). \end{aligned} \quad (5)$$

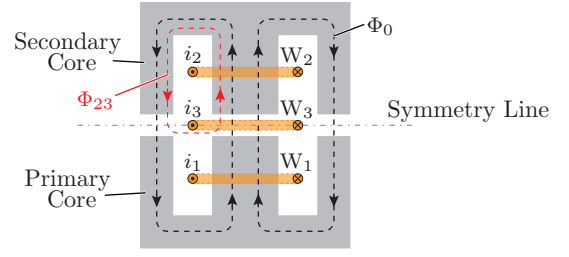


Fig. 5: WPT system with the primary winding W_1 (N_1 turns), the secondary winding W_2 (N_2 turns) and the single turn ($N_3 = 1$) SS winding. M_0 between any two of the windings is equal as flux lines always close through all three of the windings. Flux lines Φ_{23} that, for example, couple only W_2 and W_3 (denoted in red) cannot exist as this would violate magnetic symmetry. Therefore, neglecting individual stray flux components of the windings, only flux lines like Φ_0 that couple all three of the windings can exist, ensuring equal mutual coupling M_0 between W_1 , W_2 and W_3 and justifying our initial assumption.

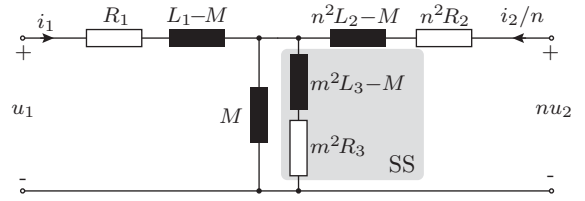


Fig. 6: Equivalent circuit of the SS WPT system. The impedance parallel to the magnetization inductance models the impact of the SS enclosure (shaded in gray).

From (5), an equivalent circuit reduced to the primary side can be derived, as shown in **Fig. 6**. The equivalent circuit is very similar to a conventional two-winding transformer equivalent circuit, except in this case there is an additional impedance in parallel to the magnetization inductance M , which represents the impact of the SS (equivalent to the modeling of core losses of conventional transformers [14]).

The value of the parameters in the equivalent circuit from **Fig. 6** can be determined from, for example, impedances calculated in 3D FEM simulation, which provides the Z-parameter values Z_{11} , $Z_{12} = Z_{21}$ and Z_{22} . The final equivalent circuit with parameters calculated for the SS WPT system from **Fig. 3**, is given in **Fig. 7**. The parameters are determined in the following way: the series branch parameters are equal to $R_0 = \Re(Z_{11} - Z_{12})$ and $L_{s0} = \Im(Z_{11} - Z_{12})/\omega$,

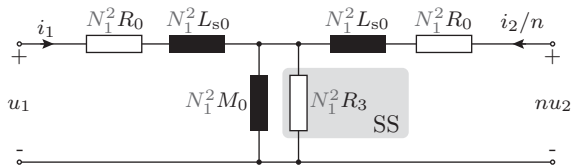


Fig. 7: Equivalent circuit for the WPT system of **Fig. 3**, valid for frequencies < 10 kHz, parameters like as calculated in 3D FEM: $R_0 = 55.6 \mu\Omega$ - DC resistance, $L_{s0} = 77.16$ nH - stray inductance, $M_0 = 172.84$ nH - mutual inductance and $R_3 = 4.97$ m Ω - SS resistance. Turns ratio $m = N_1/N_3 = N_1$, because $N_3 = 1$. It should be noted that the SS stray inductance is very low and it is neglected in the further analysis, i.e. $m^2 L_3 - M \approx 0$. In addition, note that the dissipated power in the resistor $N_1^2 R_3$ is equal to the losses in the SS plates/enclosure.

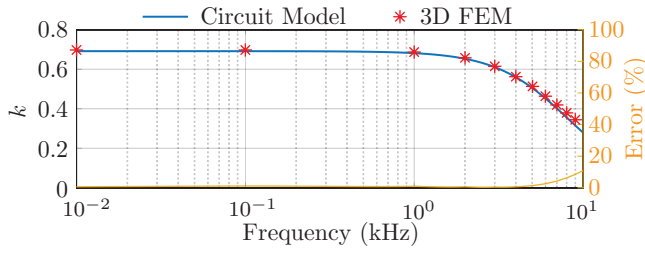


Fig. 8: Coupling coefficient k of the SS WPT system from **Fig. 3**, calculated utilizing the circuit model given in **Fig. 7**. The results are verified by comparing the model (blue line) with directly exported values from 3D FEM simulation.

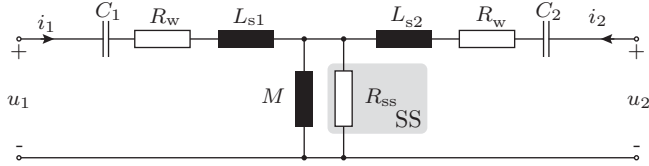


Fig. 9: Equivalent circuit with series capacitors C_1 and C_2 for resonant compensation. The parameters for a certain number of turns N_1 are: $R_w = N_1^2 R_0$, $L_{s1} = L_{s2} = N_1^2 L_{s0}$, $M = N_1^2 M_0$ and $R_{ss} = N_1^2 R_3$ (cf. **Fig. 7**).

whereas the magnetization branch parameters are obtained as $M_0 = 1/\Im(1/Z_{12}^*) \cdot 1/\omega$ and $R_3 = 1/\Re(1/Z_{12}^*)$. It should be noted that these parameters are calculated per turn, i.e., assuming $N_1 = N_2 = N_3 = 1$. This is due to FEM simulation analysis, where the winding volume is treated as a single large ‘stranded’ conductor (‘stranded’ means that no high-frequency effects are assumed in the winding volume). Therefore, if the effective parameter values for an arrangement with a specific number of turns should be calculated, the values must be scaled with N_1^2 as indicated in **Fig. 7**. For example if $N_1 = 100$, the SS resistance is $R_{ss} = 49.7\Omega$ and the winding resistance is $R_w = 0.55\Omega$.

The derived circuit model is verified by calculating the coupling coefficient $k(f) = L_{12}(f)/(L_{12}(f) + L_{s1})$ and comparing this result with $k(f)$ obtained from 3D FEM simulations. **Fig. 8** confirms a good matching between the model and 3D FEM simulation results (relative error below 10% for the considered frequency range). Therefore, the proposed equivalent circuit modeling approach allows good prediction of the SS’ influence on the inductive couplings. Note that the coupling coefficient k of the SS WPT system is relatively low, which makes resonant compensation necessary to maximize the system performance.

III. RESONANT COMPENSATION

Due to relatively low coupling coefficient k in the analyzed SS WPT system, cf. **Fig. 8**, relatively large voltage drops across the stray inductances reduce its ability to transfer power to the load. Therefore, typically in such systems resonant compensation with capacitors is employed, as explained in detail in [15], where various resonant compensation methods for WPT systems are explained. Nevertheless, in this paper we use the series-series compensation method. The equivalent circuit when implementing this compensation method is shown in **Fig. 9**, where C_1 and C_2 are series resonant compen-

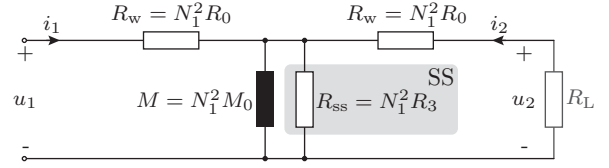


Fig. 10: Simplified SS WPT system equivalent circuit considering resonant compensation for unity turns ratio ($n = 1$). Values of the per turn parameters are given in **Fig. 7**.

sation capacitors. Typically, the capacitor values are chosen considering a resonance with the primary and secondary self-inductances, i.e., $C_1 = 1/(\omega^2 L_{11})$ and $C_2 = 1/(\omega^2 L_{22})$, where $L_{11} = (L_{s1} + L_{12})$ and $L_{22} = (L_{s2} + L_{12})$ at given frequency. Note that L_{12} is calculated from the parallel equivalent of the magnetization branch and it is frequency dependent (cf. **Fig. 14(b)**)

$$L_{12}(\omega) = \frac{M R_{ss}^2}{R_{ss}^2 + (\omega M)^2} \quad (6)$$

Also, most WPT systems are not enclosed in SS, and therefore, do not exhibit a lower resistance R_{ss} in parallel to the relatively low value of the R_{ss} , with increasing frequency ω , the magnetization reactance ωM soon reaches large values than R_{ss} , i.e. shunt branch shows an approximately resistive behavior. This is also seen from the expression for $L_{12}(\omega)$, where $\omega \rightarrow \infty$ results in $L_{12}(\omega) \rightarrow 0$. In addition to these reasons, our analysis shows that the SS losses are larger if the self-inductances are compensated, compared to only compensating for stray inductance. Note that stray inductances are constant and frequency independent for the fixed geometry, i.e. fixed placement of the primary and secondary cores of the SS WPT system. Therefore, the resonant compensation capacitors should be calculated as

$$C_1 = \frac{1}{\omega^2 L_{s1}} \quad \text{and} \quad C_2 = \frac{1}{\omega^2 L_{s2}}. \quad (7)$$

Finally, for typical WPT systems without SS enclosures, frequency has no serious impact on inductances and, therefore, compensation of stray or self-inductances can be done. It should be kept in mind that this is not the case for SS WPT systems, where frequency has serious impact on self-inductances, see (6). Therefore, since stray inductances are not impacted by the frequency, the discussed series-series resonant compensation (of the stray inductances) should be used for SS encapsulated WPT systems.

IV. OPTIMAL NUMBER OF TURNS

The influence of the number of turns N_1 on the SS WPT system parameters is shown in the equivalent circuit depicted in **Fig. 10**, which already considers resonant compensation of the stray inductances (see **Sec. III**), i.e. L_{s1} and L_{s2} are eliminated by C_1 and C_2 . From the circuit model it can be seen that increasing the number of turns N_1 increases the equivalent SS resistance R_{ss} , which advantageously reduces SS losses for the same magnetization branch. However, increasing N_1 also increases the winding resistances R_w , which results in higher winding copper losses. Therefore, an optimal number of turns $N_{1,opt}$ exists where the sum of winding and SS losses in R_w

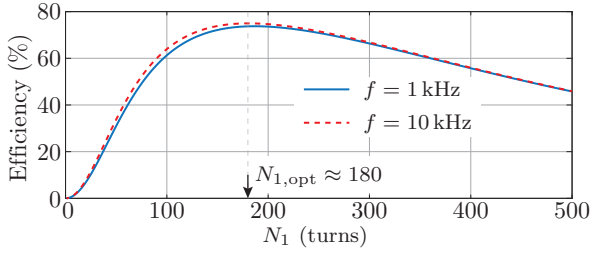


Fig. 11: Efficiency of the SS WPT system for $R_L = R_{L,nom} = 25 \Omega$, obtained by evaluating the circuit in **Fig. 10** at 1 kHz and 10 kHz. Both frequencies result in the same optimum number of turns $N_{1,opt} \approx 180$.

and R_{ss} is minimal and hence maximum WPT efficiency is achieved.

The SS WPT system should supply a load R_L as shown in **Fig. 10**. The efficiency of this power transfer depends on the circuit element values such as R_w , M , R_{ss} and R_L . As the geometry of the system is given, R_w , M and R_{ss} depend only on N_1 . Note that R_L is independent of the number of turns (it should be kept in mind that $n = 1$ is assumed). R_L is determined by the output power and voltage. Therefore, it is a sensible choice to calculate $N_{1,opt}$ for the nominal value of the load resistance given by the nominal operating point (cf. **Tab. I**) as

$$R_{L,nom} = \frac{\hat{U}_2^2}{2P_2} = 25 \Omega. \quad (8)$$

To show the impact of N_1 on the system's efficiency, the latter is calculated and shown in **Fig. 11**. It is evaluated for two different frequencies, low- and high-frequency, to show that the impact of the frequency-dependent shunt reactance ωM (cf. **Fig. 10**) can be neglected in this analysis. This allows to express $N_{1,opt}$ in a compact analytic form as

$$N_{1,opt} = \sqrt{\frac{R_{L,nom}}{\sqrt{R_0(R_0 + 2R_3)}}} \approx 180, \quad (9)$$

which verifies the result shown in **Fig. 11**. Note that in this analysis, high-frequency effects in the windings (skin and proximity effects, cf. [16]) are not considered and they can change the result for $N_{1,opt}$, due to their frequency-dependent influence on the winding resistance R_0 . However, even in the presence of high-frequency effects, the maximum efficiency achievable under these circumstances and for a given N_1 can still be achieved by controlling the load resistance R_L to the value that maximizes efficiency. Such load resistance value is discussed in **Sec. V**.

V. HARDWARE PROTOTYPE AND MODEL VERIFICATION

A. High-Frequency Effects in the Windings

As shown in the previous **Sec. IV**, for a given load resistance R_L there is an optimum number of turns N_1 that results in maximum WPT efficiency. Depending on the output voltage \hat{U}_2 and the required output power P_2 , the load resistance may take different values during operation. However, the nominal value $R_L = R_{L,nom}$ (cf. (8)) is used when choosing the number of turns N_1 for the prototype. For the required nominal values (see **Tab. I**), the prototype is realized with

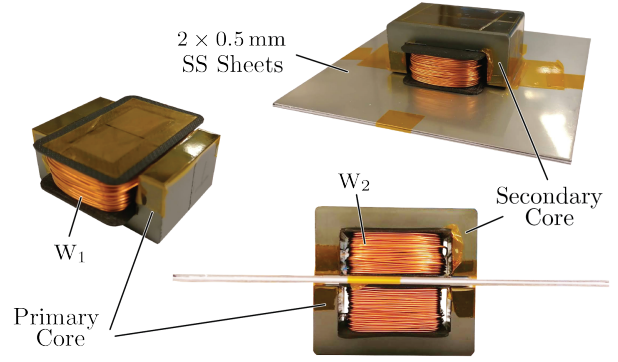


Fig. 12: SS WPT system hardware demonstrator realized with $N_1 = N_2 = 180$ turns made of 0.5 mm diameter wire. The primary and secondary cores consist of 2 stacked E 47/20/16 N87 ferrite cores [11].

TABLE II: SS WPT Model Parameters.

Parameter	3D FEM	Prototype	Rel. Error
$R_{w,dc}$	1.8 Ω	1.9 Ω	5.3 %
L_s	2.5 mH	2.62 mH	4.6 %
M	5.6 mH	5.4 mH	3.7 %
R_{ss}	160 Ω	155 Ω	3.2 %

$N_1 = N_{1,opt} = 180$ turns, cf. **Fig. 11** and (9). Given the winding window area of the considered core (cf. **Fig. 3**), the feasible diameter of the used wire is 0.5 mm. The prototype is presented in **Fig. 12**. To verify the 3D FEM analysis and the model of the SS WPT system, the impedances Z_{11} , Z_{12} and Z_{22} of the prototype are measured with an impedance analyzer [17]. Similarly as in **Sec. II**, the parameters of the circuit model are determined based on the measured impedances and given in **Tab. II**, where $L_{s1} = L_{s2} = L_s$. Also in **Tab. II**, the measured parameters are compared with the ones calculated from the 3D FEM simulation results. The relative error between is relatively low, which verifies the 3D FEM analysis results and the parametrization of the circuit model based on the these simulation results.

Importantly, in the frequency range where the SS WPT system should operate (up to 10 kHz), high-frequency effects in the windings, such as skin and proximity effects, cf. [16], must be considered. The skin effect can be calculated in a relatively simple way by using the function $F_R(f)$ given in (11) in the **Appendix**. The increase of the winding resistance with frequency due to the skin effect is considered by multiplying the DC resistance with the factor $2F_R(f)$, i.e., $R_{w,dc} \cdot 2F_R(f)$. The function $F_R(f)$ is monotonically increasing with frequency f and $F_R(10 \text{ kHz}) = 0.5002$. Therefore, the increase of the winding resistance due to skin effect is very low (factor of $2 \cdot 0.5002 = 1.0004$) even at the upper range of the considered operating frequency range and can therefore be neglected. The loss increase caused by the proximity effect can be modeled as an additional winding resistance component $R_{w,dc} 2G_R(f) \cdot H^2$, whereby $G_R(f)$ is given in (13) in the **Appendix**. Thus, the total winding resistance is $R_w(f) = R_{w,dc}(1 + 2G_R(f) \cdot H^2)$. The factor H^2 depends on the field strength, the winding current, and the distribution of the individual turns, cf. [16]. As the increase of

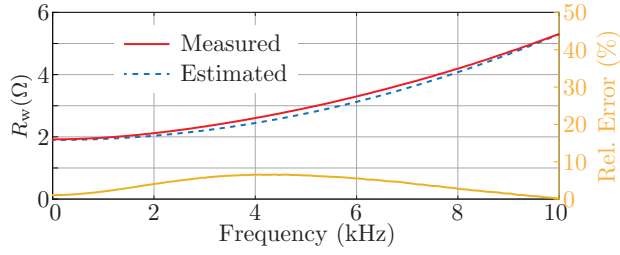


Fig. 13: Measured and estimated AC resistance of the SS WPT system winding, which is the same for the primary and the secondary winding, i.e. $R_{w1} = R_{w2} = R_w$.

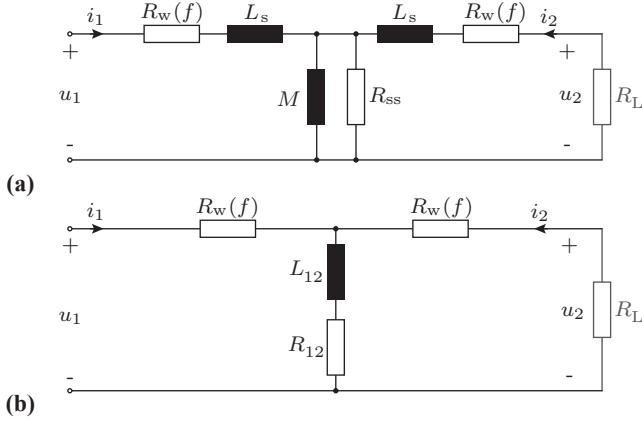


Fig. 14: (a) Model of the SS WPT prototype used for evaluating power measurements. The model considers frequency-dependent winding resistances $R_w(f)$ according to the estimation shown in **Fig. 13**, stray inductances $L_s = 2.62$ mH, a mutual inductance $M = 5.4$ mH, and the SS equivalent resistance $R_{ss} = 155$ Ω . (b) SS WPT system model with resonant compensation. At an excitation frequency of $f = 2250$ Hz, the values of the elements are $R_w = 2.07$ Ω , $R_{12} = 26.68$ Ω and $L_{12} = 4.14$ mH. The resonant capacitors (cf. **Fig. 9**) are equal to $C_1 = C_2 = 1.9$ μ F.

the winding resistance due to proximity effect is a topic very well studied in literature, the detailed theoretical calculation of H^2 is omitted in this paper, and it is estimated from the impedance measurements on the prototype instead. Namely, using the value of the winding resistance measured at 10 kHz, we find $H^2 = (R_w(10 \text{ kHz})/R_{w,dc} - 1)/(2G_R(10 \text{ kHz})) = 1.3862 \times 10^8 \text{ A}^2/\text{m}^2$. With all the considerations above, the measured and estimated winding resistance versus frequency is shown in **Fig. 13**. The relative error between the measured and the value estimated using $G_R(f)$ is sufficiently low and stays below 10%. The estimated value of the winding resistance is used for the circuit model in the further analysis.

Finally, for the verification of the power measurements of the SS WPT system, the circuit model given in **Fig. 14(a)** is used. After resonant compensation of the stray inductances (cf. **Sec. III**), the model is transfigured into the one shown in **Fig. 14(b)**, where the series equivalent of the shunt branch is used, i.e., R_{12} and L_{12} instead of M and R_{ss} , as this facilitates the derivation of simpler analytical expressions (e.g. for output power, efficiency or SS losses).

B. Optimal Excitation Frequency and Load Resistance

When considering the operating frequency of the SS WPT system, the circuit model from **Fig. 14(b)** with the frequency-dependent winding resistances $R_w(f)$ is used. A low exci-

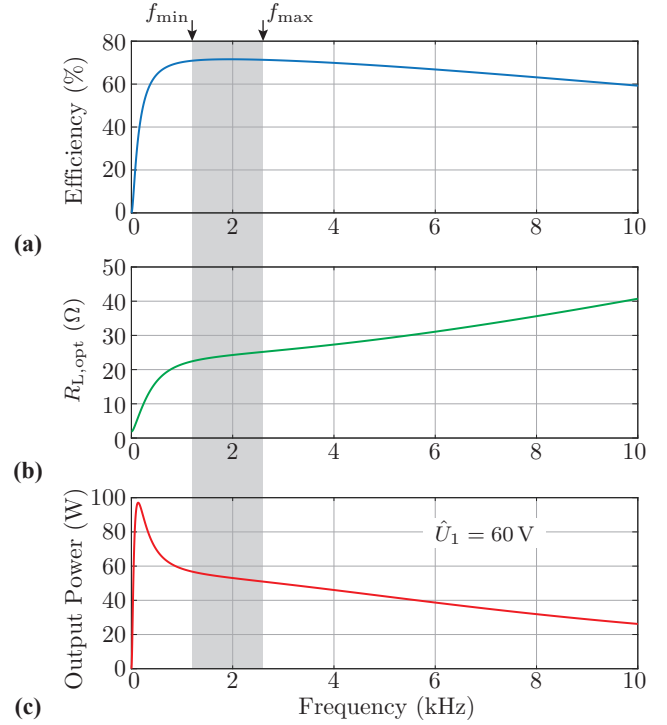


Fig. 15: (a) Efficiency of the SS WPT system versus frequency, calculated from the circuit model given in **Fig. 14(a)**. Resonant compensation of the stray inductances is applied. The maximum efficiency is 71.2% at 1.935 kHz. (b) For each frequency, the optimum resistance $R_L = R_{L,opt}$ is calculated that ensures maximum possible efficiency. Therefore, the output power for a fixed input voltage $\hat{U}_1 = 60$ V varies with frequency (cf. (c)). The shaded area indicates the region around the maximum efficiency point, where the efficiency deviates not more than 0.1% from maximum value.

tation frequency results in low magnetization reactance, and therefore, in large magnetization current that causes large losses in the primary winding and reduces the efficiency. On the other hand, a high excitation frequency results in a high winding resistance that results in high winding losses and again in reduced efficiency. Therefore, there is a frequency between these two values that gives maximum efficiency. To determine this frequency, the efficiency of the circuit model from **Fig. 14(b)** is calculated and shown in **Fig. 15**. As expected, the efficiency increases from small values at low frequencies and, after reaching a maximum value, starts dropping with increasing frequency. Since the efficiency maximum is relatively flat, the acceptable region of frequencies for the operation of the SS WPT system is between $f_{min} = 1.6$ kHz and $f_{max} = 2.3$ kHz, where the efficiency only deviates by 0.1% from the maximum value. This flexibility regarding the optimum operating frequency is beneficial, as the resonant compensation cannot be done perfectly due to parasitics and capacitor tolerances.

When the efficiency in **Fig. 15(a)** is calculated, it is necessary to adapt the load resistance R_L with frequency to the value that ensures the maximum WPT efficiency at that frequency, since the winding resistance $R_w(f)$ changes with frequency (cf. **Fig. 13**) and deviates from the value used to calculate the optimum number of turns (cf. **Sec. IV**). Therefore, based on the circuit model from **Fig. 14(b)**, similar to the analytic expression (9) for the optimal number of turns

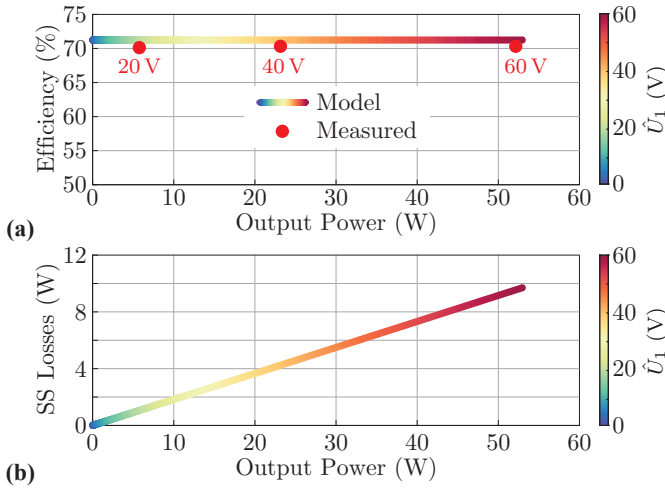


Fig. 16: Output power control by changing the input voltage \hat{U}_1 , where the load resistance is kept constant and equal to its optimal value $R_{L,\text{opt}} \approx 24 \Omega$ that results in maximum possible efficiency, cf. **Fig. 15**. (a) The efficiency stays constant over output power and equal to the maximum value of $\approx 71.2\%$. Three measurements points for different voltages $\{20 \text{ V}, 40 \text{ V}, 60 \text{ V}\}$ verify the model calculations. (b) The ratio of the SS losses and the output power is constant when the load resistance does not change, cf. (19). Therefore, the SS losses increase linearly with the output power.

$N_{1,\text{opt}}$, the expression for the optimal load resistance is derived as

$$R_{L,\text{opt}} = \frac{\sqrt{R_w} \sqrt{R_w^2 + 3R_w R_{12} + 2R_{12}^2} + 2(\omega L_{12})^2}{\sqrt{R_w} + R_{12}}. \quad (10)$$

Note that $R_{L,\text{opt}}$ depends on frequency via ωL_{12} and also because of $R_w(f)$. Its value versus frequency is shown in **Fig. 15(b)**. It should be noted that this formula is utilized for the efficiency and output power calculation in **Fig. 15**. At 1.935 kHz, the maximum efficiency with a load resistance 24.16Ω is achieved, which is close to its nominal value $R_{L,\text{nom}} = 25 \Omega$ since the winding resistance stays close to its DC value at this frequency (cf. **Fig. 13**) and **Sec. IV**.

The output power for a fixed input voltage of $\hat{U}_1 = 60 \text{ V}$ is shown in **Fig. 15(c)**, which at 1.935 kHz results in an output power of around 53 W, which is close to the nominal power. Therefore, at this operating point, the output voltage is close to its nominal value as well, i.e., $\hat{U}_2 \approx 50 \text{ V}$. Note that, due to the voltage drop over the winding resistances R_w , there is a difference between the input voltage \hat{U}_1 and the output voltage \hat{U}_2 .

For availability reasons, film capacitors of $C_1 = C_2 = 1.9 \mu\text{F}$ are used for resonant compensation, which results in a resonant frequency of $f = 2250 \text{ Hz}$. Power measurements are done at this frequency and the model in **Fig. 14(b)** is used for verification of these measurements.

C. Output Power Control Methods

The output power P_2 of the SS WPT system is the power delivered to the secondary at voltage \hat{U}_2 . Therefore, the power receiver modeled by the load resistance should be calculated as $R_L = \hat{U}_2 / (2P_2)$. As discussed previously, for a given power, the load resistance R_L can be controlled by changing \hat{U}_2 , which requires an additional DC/DC converter [18], and

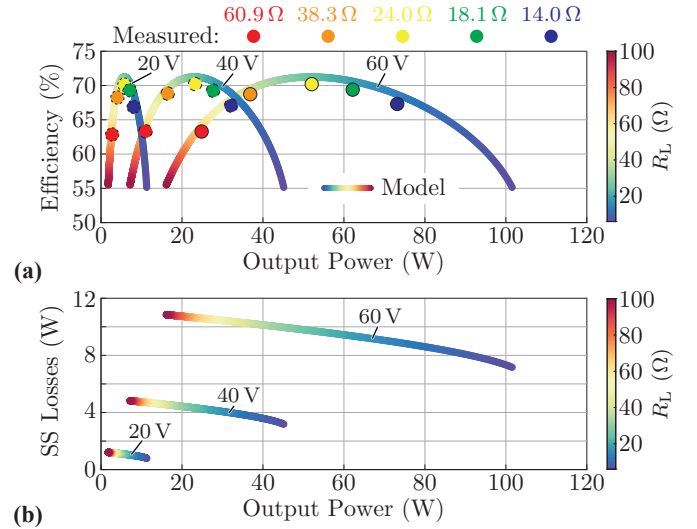


Fig. 17: Output power control by changing the load resistance R_L . Three curves for the input voltages of $\hat{U}_1 = \{20 \text{ V}, 40 \text{ V}, 60 \text{ V}\}$ are shown. (a) The efficiency over output power is not constant since the load resistance R_L changes. The efficiency is maximal when the load resistance is equal to its optimal value $R_{L,\text{opt}} \approx 24 \Omega$. For each input voltage, five power measurement points with different load resistances are denoted by dots, whereby the dots' colors indicate the values of the load resistance. (b) SS losses versus output power for different input voltages. With this control approach, SS losses reduce with increasing output power. This dependence is reflected by the analytic expression (19).

it is typically set to a value $R_L = R_{L,\text{opt}}$ that ensures the maximum WPT efficiency, cf. (10). In such a scenario, the output power can be controlled by changing the input voltage \hat{U}_1 , as shown in **Fig. 16(a)**. It should be noted that efficiency does not depend on the input voltage \hat{U}_1 , though only on the parameters of the circuit model (cf. **Fig. 14(b)**), which is also shown by the analytic expression for the efficiency (20). The model results for the efficiency in **Fig. 16(a)** are verified with three power measurements at different input voltages, $\hat{U}_1 = \{20 \text{ V}, 40 \text{ V}, 60 \text{ V}\}$, which are denoted with red dots.

An important practical aspect is to keep the temperature of the SS enclosure limited, e.g., to prevent injuries if a human touches the enclosure surface. This can be achieved by keeping the SS losses P_{ss} limited, since they mainly heat up the SS enclosure. The SS losses may be obtained by calculating the power of the resistor R_{ss} (see circuit model in **Fig. 14(a)**) or equivalently R_{12} (see circuit model in **Fig. 14(b)**). Therefore, it is clear that at a given operating frequency, the SS losses P_{ss} would increase proportionally to the square of the input voltage \hat{U}_1 , similar as the output power P_2 , which is shown by the analytic expressions (17) and (16). When the load resistance R_L is constant, the ratio of the SS losses and the output power is constant (cf. (19)), resulting in SS losses linearly increasing with the output power, cf. **Fig. 16(b)**. By using (19), for the analyzed operating point we find $P_{\text{ss}}/P_2 \approx 0.18$, which corresponds to the slope of the line shown in **Fig. 16(b)**.

In case WPT should not be done at maximum efficiency, the output power can also be controlled by changing the load resistance R_L . Such characteristics are shown in **Fig. 17**. This control method can be preferred in cases where large output power should be delivered, but increasing the input

voltage would not be possible, due to, e.g., too high SS losses. Note that with this control method, SS losses would reduce when increasing the output power (cf. **Fig. 17(b)**), where the opposite applies if the input voltage is increased (cf. **Fig. 16(b)**). This is actually intuitive if the equivalent circuit in **Fig. 14(b)** is observed. A smaller load resistance R_L takes more current and therefore causes a larger voltage drop across the winding resistance R_w . This, in turn, reduces the voltage across the SS resistance R_{ss} , indicating a reduction of the SS losses.

Finally, two power control methods are possible: (1) Power control by keeping the load resistance equal to its nominal value $R_L = R_{L,nom}$ and changing the input voltage \hat{U}_1 (cf. **Fig. 16**). This ensures always maximum efficiency but the SS losses increase linearly with the output power. (2) Power control by changing the load resistance, where maximum efficiency cannot be guaranteed anymore, but the SS losses can even be reduced for larger output power (cf. **Fig. 17**).

VI. CONCLUSIONS AND FUTURE WORK

This paper analyzes a wireless power transfer (WPT) system with stainless-steel (SS) enclosure, i.e., WPT through conductive SS sheets and/or pushing power through SS walls (PTW). From the given geometry of the system, the impact of the SS on the WPT is first clarified with 3D FEM simulations, where, e.g., distributions of flux densities and induced eddy currents are obtained. From the eddy current distribution, a model of the system where the SS is replaced by a short-circuited single turn winding is proposed. This leads to a very effective and simple electrical equivalent circuit model, where finally the impact of the SS can be modeled with a resistor in parallel to the magnetization inductance like typically found for core losses in conventional transformer equivalent circuits.

The proposed model allows to first identify resonant series-compensation of the stray inductances as favorable compared to compensating the self-inductances like often done in WPT systems without SS. Furthermore, we then derive an analytic expression for the optimal number of turns that results in maximum efficiency at a given nominal operating point. Similarly, for a given system it becomes possible to derive an optimum load resistance that maximizes the efficiency. A prototype of the system for 50 W output power at 50 V secondary voltage is built and its measured circuit model parameters are used to verify the 3D FEM simulation results. The relative error is below 5.5%. The operating frequency of the prototype is 2250 Hz; higher values are less attractive due to the increased winding resistance as a consequence of the proximity effect.

Further verification of the SS WPT system model is done by power measurements, where two power control approaches are studied: (1) power control by changing the input voltage, which allows keeping the efficiency at its maximum of 71.2% and (2) power control by changing the load resistance, which allows to limit the losses in the SS. The measurement results match closely with the model calculations.

Further work is focused on reducing the SS effect on the WPT system by introducing cuts in the SS sheets that interrupt the induced eddy current loops and, therefore, increase the equivalent resistance of the SS, which finally leads to lower losses in the SS and up to 10% higher WPT efficiency.

APPENDIX

A. Formulas for the Skin and Proximity Effects

The formulas for calculating $F_R(f)$ and $G_R(f)$ are taken from [16]:

$$F_R(f) = \frac{\xi}{4\sqrt{2}} \left[\frac{\text{num}_{FR}(\xi)}{\text{Br}_1(\xi)^2 + \text{Bi}_1(\xi)^2} \right] \quad (11)$$

$$\text{num}_{FR}(\xi) = \text{Br}_0(\xi)\text{Bi}_1(\xi) - \text{Br}_0(\xi)\text{Br}_1(\xi) - \text{Bi}_0(\xi)\text{Br}_1(\xi) - \text{Bi}_0(\xi)\text{Bi}_1(\xi) \quad (12)$$

$$G_R(f) = -\frac{\xi\pi^2 d^2}{2\sqrt{2}} \left[\frac{\text{num}_{GR}(\xi)}{\text{Br}_0(\xi)^2 + \text{Bi}_0(\xi)^2} \right], \quad (13)$$

$$\text{num}_{GR}(\xi) = \text{Br}_2(\xi)\text{Br}_1(\xi) + \text{Br}_2(\xi)\text{Bi}_1(\xi) + \text{Bi}_2(\xi)\text{Bi}_1(\xi) - \text{Bi}_2(\xi)\text{Br}_1(\xi) \quad (14)$$

$$\xi = \frac{d}{\sqrt{2}\delta} \quad \text{and} \quad \delta = \frac{1}{\sqrt{\pi\mu_0\sigma f}}, \quad (15)$$

where $\text{Br}_n(\xi) = \Re(\text{J}_n(\xi \cdot e^{j3\pi/4}))$ and $\text{Bi}_n(\xi) = \Im(\text{J}_n(\xi \cdot e^{j3\pi/4}))$ are n -th order Kelvin functions and J_n is the n -th order Bessel function, d is the wire diameter, σ is the copper wire conductivity and f is the electrical frequency.

B. Output Power and SS Losses

Based on the circuit model in **Fig. 14(b)**, the output power P_2 is equal to

$$P_2 = \frac{1}{2} \frac{R_L(R_{12}^2 + X_{12}^2)}{\text{den}_p} \cdot \hat{U}_1^2, \quad (16)$$

and the SS losses P_{ss} are equal to

$$P_{ss} = \frac{1}{2} \frac{R_{12}(R_L + R_w)^2}{\text{den}_p} \cdot \hat{U}_1^2, \quad (17)$$

where $X_{12} = \omega L_{12}$ and

$$\text{den}_p = (R_{12}R_L + 2R_{12}R_w + R_LR_w + R_w^2)^2 + X_{12}^2(R_L + 2R_w)^2. \quad (18)$$

Therefore, the ratio of the SS losses and the output power is equal to

$$\frac{P_{ss}}{P_2} = \frac{R_{12}(R_L + R_w)^2}{R_L(R_{12}^2 + X_{12}^2)}. \quad (19)$$

C. Efficiency of the SS WPT System

The expression for the efficiency of the SS WPT system is derived from the the circuit model given in **Fig. 14(b)** as $\eta = P_2/P_1$, and it is equal to

$$\eta = \frac{R_L(R_{12}^2 + X_{12}^2)}{\text{den}}, \quad (20)$$

$$\begin{aligned} \text{den} = & R_{12}^2 R_L + 2 R_{12}^2 R_w + R_{12} R_L^2 + 4 R_{12} R_L R_w + \\ & 3 R_{12} R_w^2 + R_L^2 R_w + 2 R_L R_w^2 + R_L X_{12}^2 + R_w^3 + \\ & 2 R_w X_{12}^2 \end{aligned} \quad (21)$$

The output power is calculated as $P_2 = 0.5 R_L \hat{I}_2^2$, and the input power as $P_1 = 0.5 \cdot \Re(\underline{U}_1 \underline{I}_1^*)$.

REFERENCES

- [1] Z. Zhang, H. Pang, A. Georgiadis, and C. Cecati, "Wireless Power Transfer—An Overview," *IEEE Transactions on Industrial Electronics*, vol. 66, no. 2, pp. 1044–1058, 2018.
- [2] R. Bosshard and J. W. Kolar, "Inductive Power Transfer for Electric Vehicle Charging: Technical Challenges and Tradeoffs," *IEEE Power Electronics Magazine*, vol. 3, no. 3, pp. 22–30, 2016.
- [3] O. Knecht, R. Bosshard, and J. W. Kolar, "High-Efficiency Transcutaneous Energy Transfer for Implantable Mechanical Heart Support Systems," *IEEE Transactions on Power Electronics*, vol. 30, no. 11, pp. 6221–6236, 2015.
- [4] Y. Zhou, C. Liu, and Y. Huang, "Wireless Power Transfer for Implanted Medical Application: A Review," *Energies*, vol. 13, no. 11, p. 2837, 2020.
- [5] M. Yamakawa, Y. Mizuno, J. Ishida, K. Komurasaki, and H. Koizumi, "Wireless Power Transmission into a Space Enclosed by Metal Walls Using Magnetic Resonance Coupling," *Wireless Engineering and Technology*, 2014.
- [6] D.-X. Yang, Z. Hu, H. Zhao, H.-F. Hu, Y.-Z. Sun, and B.-J. Hou, "Through-Metal-Wall Power Delivery and Data Transmission for Enclosed Sensors: A Review," *Sensors*, vol. 15, no. 12, pp. 31 581–31 605, 2015.
- [7] C. Van Pham, A.-V. Pham, and C. S. Gardner, "Development of Helical Circular Coils for Wireless Through-Metal Inductive Power Transfer," in *Proc. of the IEEE Wireless Power Transfer Conference (WPTC)*, 2017, pp. 1–3.
- [8] H. Zhang, L. Ding, N. Liu, F. Yang, and L. Qian, "Optimal Operating Frequency of Inductive Power Transfer Through Metal Barriers," in *Proc. of the 89th IEEE Vehicular Technology Conference (VTC-Spring)*, 2019, pp. 1–5.
- [9] H. Ishida, T. Kyoden, and H. Furukawa, "Super-Low Frequency Wireless Power Transfer with Lightweight Coils for Passing Through a Stainless Steel Plate," *Review of Scientific Instruments*, vol. 89, no. 3, 2018.
- [10] R. V. Giuffrida, S. Mirić, D. Bortis, and J. W. Kolar, "Looking Through Walls"—Actuator Position Measurement Through a Conductive Wall," in *Proc. of the 23rd IEEE International Conference on Electrical Machines and Systems (ICEMS)*, 2020, pp. 1649–1654.
- [11] EPCOS AG - TDK, *Ferrites and Accessories, E 47/20/16 Core, Series/Type: B66383, Datasheet*, 2017.
- [12] L. Huang, J. Zou, Y. Zhou, Y. Hong, J. Zhang, and Z. Ding, "Effect of Vertical Metal Plate on Transfer Efficiency of the Wireless Power Transfer System," *Energies*, vol. 12, no. 19, p. 3790, 2019.
- [13] C. Sun, N. H. Kutkut, D. Novotny, and D. Divan, "General Equivalent Circuit of a Multi-Winding Co-Axial Winding Transformer," in *Proc. of the 30th IEEE Industry Applications Society Annual Conference (IAS)*, vol. 3, 1995, pp. 2507–2514.
- [14] C. W. T. McLyman, *Transformer and Inductor Design Handbook*. 4th ed. Boca Raton: CRC press, doi: 10.1201/b10865, 2017.
- [15] R. Bosshard, "Multi-Objective Optimization of Inductive Power Transfer Systems for EV Charging," Ph.D. dissertation, ETH Zurich, 2015.
- [16] J. Biela, "Optimierung des elektromagnetisch integrierten Serien-Parallel Resonanzkonverters mit eingepprägtem Ausgangsstrom (in German)," Ph.D. dissertation, ETH Zurich, 2005.
- [17] OMICRON LAB, *Vector Network Analyzed - Bode 100, 1 Hz to 50 MHz, Technical data sheet*, 2021.
- [18] R. Bosshard, J. W. Kolar, and B. Wunsch, "Control Method for Inductive Power Transfer with High Partial-Load Efficiency and Resonance Tracking," in *Prof. of the International Power Electronics Conference (IPEC / ECCE ASIA)*, 2014, pp. 2167–2174.